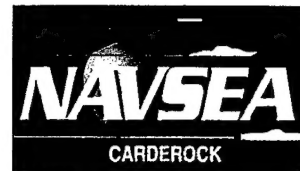


**Carderock Division  
Naval Surface Warfare Center**

West Bethesda, Maryland 20817-5700



NSWCCD-50-TR-2002 / 019 February 2002

Hydromechanics Directorate  
Research and Development Report

**PIV Measurements of the Cross-Flow Velocity Field  
Around a Turning Submarine Model (ONR Body-1)  
Part I: Experimental Setup**

by

Thomas C. Fu  
Paisan Atsavapranee  
David E. Hess



Approved for public release: distribution unlimited.

20020514 110

# REPORT DOCUMENTATION PAGE

*Form Approved  
OMB No. 0704-0188*

Public reporting burden for this collection of information is estimated to average 1 hour per response, including the time for reviewing instructions, searching existing data sources, gathering and maintaining the data needed, and completing and reviewing the collection of information. Send comments regarding this burden estimate or any other aspect of this collection of information, including suggestions for reducing this burden to Washington Headquarters Services, Directorate for Information, Operations and Reports, 1215 Jefferson Davis Highway, Suite 1204, Arlington, VA 22202-4302, and to the Office of Management and Budget, Paperwork Reduction Project (0704-0188), Washington, DC 20503.

<b>1. AGENCY USE ONLY (Leave blank)</b>			<b>2. REPORT DATE</b> February 2002		<b>3. REPORT TYPE AND DATES COVERED</b> Final	
<b>4. TITLE AND SUBTITLE</b> PIV Measurements of the Cross-Flow Velocity Field Around a Turning Submarine Model (ONR Body-1)			<b>5. FUNDING NUMBERS</b>			
<b>6. AUTHOR(S)</b> Thomas C. Fu, Paisan Atsavapranee and David E. Hess						
<b>7. PERFORMING ORGANIZATION NAME(S) AND ADDRESS(ES)</b> Carderock Division, Naval Surface Warfare Center Code 5600 9500 MacArthur Boulevard West Bethesda, Maryland 20817-5700			<b>8. PERFORMING ORGANIZATION REPORT NUMBER</b> NSWCCD-50-TR-2002 / 019			
<b>9. SPONSORING / MONITORING AGENCY NAME(S) AND ADDRESS(ES)</b> Dr. L. Patrick Purtell Office of Naval Research 800 North Quincy Street Arlington, VA 22217-5660 703-696-4308			<b>10. SPONSORING / MONITORING AGENCY REPORT NUMBER</b> Dr. Thomas T. Huang Newport News Shipbuilding Airport Plaza One, Suite 100 2711 South Jefferson Davis Highway Arlington, VA 22202-4028 703 416 2838			
<b>11. SUPPLEMENTARY NOTES</b>						
<b>12a. DISTRIBUTION / AVAILABILITY STATEMENT</b> Approved for public release: distribution unlimited.			<b>12b. DISTRIBUTION CODE</b>			
<b>13. ABSTRACT (Maximum 200 words)</b> <p>Particle Image Velocimetry (PIV), a quantitative flow visualization technique, was utilized to characterize the flow field around a sting-mounted captive model in a steady turn. The submarine model (ONR Body-1) was also instrumented with block gages, yielding force and moment data in tandem with the detailed map of the cross-flow velocity field. The near wake flow field is observed to be dominated by complex interactions of large-scale vortical structures from the hull separated flow and the tip vortices from the sail and various control surfaces. In addition, the incorporation of micro-vortex generators (MVGs) on the submarine model is shown to have significant effects on the flow field and the resulting forces and moments on the submarine model.</p>						
<b>14. SUBJECT TERMS</b> Particle Image Velocimetry, flow visualization, micro-vortex generators, Submarine maneuvering			<b>15. NUMBER OF PAGES</b> 30+iv		<b>16. PRICE CODE</b>	
<b>17. SECURITY CLASSIFICATION OF REPORT</b> Unclassified		<b>18. SECURITY CLASSIFICATION OF THIS PAGE</b> Unclassified		<b>19. SECURITY CLASSIFICATION OF ABSTRACT</b> Unclassified		
<b>20. LIMITATION OF ABSTRACT</b> Unclassified						

**THIS PAGE INTENTIONALLY LEFT BLANK**

## **Contents**

Abstract .....	1
Administrative Information.....	1
Introduction .....	1
Particle Image Velocimetry (PIV) .....	3
Experimental Set-Up .....	5
Force and Moment Measurements .....	15
Results and Discussion.....	21
Conclusions .....	25
Acknowledgments.....	26
References .....	27

## **Figures**

1. Laser sheet position (data planes) relative to the model as it passes through the turn.....	3
2. Dye injectors and boundary layer trip wire .....	7
3. Sting-mounted Submarine for Rotating Arm Testing.....	8
4. Sketch showing standard submarine coordinate system and positive directions of angles, velocities, forces and moments.....	9
5. Cross-sectional view of Rotating Arm facility.....	9
6. Sketch showing relationships between yaw angles and radii .....	10
7. Sketch showing MVG locations for Config. 2 .....	11
8. Submerged PIV instrumentation deployed in the Rotating Arm Basin.....	13
9. PIV instrumentation: image acquisition and laser systems .....	14
10. Camera lens optics and submersible enclosure .....	14
11. Cross-cut velocity and vorticity field, no MVGs .....	23
12. Cross-cut velocity and vorticity field, with MVGs .....	24

## Tables

1. Locations ( $x_1, y_1, z_1$ ) and orientations ( $x_2, y_2, z_2$ ) of the inboard set of measurement planes, in model coordinates (ft). The left column represents the plane number, starting from the rightmost plane as shown in Figure 1.....	4
2. Longitudinal distance from model FP to MVG TE.....	11
3. Equations to determine hydrodynamic coefficients from measured coefficients for rotating arm sting experiments. ....	18
4. Constants to be used in the equations shown in Table 2.....	19
5. Dimensionless Force and Moment Measurements for Config. 1.....	20
6. Dimensionless Force and Moment Measurements for Config. 2.....	20
7. Dimensional Force and Moment Measurements for Config. 1 in <i>lbs</i> and <i>ft-lbs</i> , respectively .....	20
8. Dimensional Force and Moment Measurements for Config. 2 in <i>lbs</i> and <i>ft-lbs</i> , respectively .....	20

## ABBREVIATIONS

CFD	computational fluid dynamics
FP	forward perpendicular
H/HTC	Hydrodynamics/Hydroacoustic Technology Center
JHU	The Johns Hopkins University
MECL	Motorola emitter-coupled logic
MVG	micro-vortex generator
NACA	National Advisory Committee for Aeronautics
NAVSEA	Naval Sea Systems Command
NSWCCD	Naval Surface Warfare Center, Carderock Division
ONR	Office of Naval Research
PIV	particle image velocimetry
ppm	parts per million
RCM	radio-controlled model
TE	trailing edge

## **ABSTRACT**

Particle Image Velocimetry (PIV), a quantitative flow visualization technique, was utilized to characterize the flow field around a sting-mounted captive model in a steady turn. The submarine model (ONR Body-1) was also instrumented with block gages, yielding force and moment data in tandem with the detailed map of the cross-flow velocity field. The near wake flow field is observed to be dominated by complex interactions of large-scale vortical structures from the hull separated flow and the tip vortices from the sail and various control surfaces. In addition, the incorporation of micro-vortex generators (MVGs) on the submarine model is shown to have significant effects on the flow field and the resulting forces and moments on the submarine model.

## **ADMINISTRATIVE INFORMATION**

This work was performed at the Naval Surface Warfare Center, Carderock Division, West Bethesda, MD 20817 and was sponsored in part by the ONR Body 1 Unclassified RCM Experiment Task of the FY00 6.2 Submarine Maneuvering and Control, WRN: N0001400-WX-20383. Additional funding was provided by Newport News Shipbuilding from their ILIR program. The Program Manager at NSWCCD is Dr. In-Young Koh, and the Program Manager at Newport News Shipbuilding is Dr. Thomas Huang. The Project Leader at the Naval Surface Warfare Center, Carderock Division is Dr. Thomas Fu of the Maneuvering and Control Department (Code 5600).

## **INTRODUCTION**

The wake of a maneuvering submarine represents a highly complex three-dimensional flow field, dominated by interactions of large-scale vortical structures from the separated flow around the body and the trailing flow structures from the sail and various control surfaces. As a submarine progresses through a maneuver, the local flow incidence angle changes in an unsteady manner, further complicating the flow interactions. In a steady turn, for instance, the asymmetric flow separation over the hull creates a pair of body vortices on the lee side. Additionally, the sail and the control surfaces of the submarine create tip vortices, whose location and strength depend upon characteristics of the local flow field and the control surface deflections. The complex interaction of these various vortical structures presents a particular difficulty in the prediction of such flows using computational fluid dynamics (CFD). Detailed measurements of the flow field not only provide validation data for CFD codes but also give physical insights into this complex flow field.

Though flow field measurements of a free-running radio-controlled model (RCM) in a maneuver using particle image velocimetry (PIV) can be preformed, there is a substantial associated increase in the complexity and cost. Steady turn conditions, being somewhat easier to compute and interpret, offer a reasonable starting point. The present study utilized a captive model mounted on a rotating arm (towing carriage) with the speed, yaw, pitch, roll and turning rate fixed through the duration of a turn. Force and

moment data, as well as the velocity field data, were measured concurrently, allowing for more complete validation of CFD codes. The test conditions, including yaw, speed, rudder and rudder angle, were chosen to match those measured from the RCM while performing a steady turning maneuver. Additionally, the effect of micro-vortex generators (MVGs) is examined. MVGs are a NASA-developed, passive, flow control device. These low aspect-ratio, lifting surfaces, with span smaller than the turbulent boundary layer thickness, were mounted downstream of the sail, on the crown of the submarine. The MVG array produces a series of streamwise trailing vortices that affect the cross-flow in a manner that effectively enhances the controllability of a submarine while undergoing a hard turn.<sup>1</sup>

A PIV system was previously built and used in the Rotating Arm Basin in 1994, to measure vortical structures from a turning submarine.<sup>2</sup> Although this test successfully demonstrated the potential of PIV technology in such an application, it also revealed the limitations of the technology at that time. Transitioning PIV from small-scale laboratory applications to large-scale facilities or field measurements involves a number of technical issues related to the deployment of a complex measurement system in a relatively remote and uncontrolled environment. These technical issues include laser power limitation and delivery technique, feasibility of utilizing scientific-grade instruments in a submerged environment, experimental physical arrangement and layout, and image acquisition and analysis issues. Since then, affordable higher power lasers, fiber optics delivery systems, digital cameras, image acquisition systems and analysis software have all became incorporated into state-of-the-art PIV systems, addressing the limitations encountered in the 1994 test. Utilizing a PIV system developed and built by the Johns Hopkins University,<sup>3,4</sup> a similar test was performed. The PIV measurements taken in this study provide detailed cross-flow velocities in a static measurement plane on the leeward side of the model as it passes by in a turn. Since the maneuver is steady, the time series of velocities in the measurement plane are equivalent to instantaneous "snapshots" of the cross flow velocity field at several axial locations relative to the model (see Fig. 1). Note that the measurement planes, as represented in Figure 1, are oriented in a changing fashion at successive stations along the model, due to the fact that the model, which is pitched, rolled and yawed, passes through a static measurement plane along a circular arc. Also, note that PIV measurements are taken using two cameras. The measurement plane for the first camera (situated inboard and closer to the model) is shown in red. The measurement plane for the second camera is shown in light green. The area of overlap between the first and second camera is shown in yellow. Only data from the inboard camera will be shown in this report. The location for each measurement plane, in model coordinates, is defined as a vector from the model reference point to the center of the measurement plane. The measurement plane orientation is defined as a unit vector, in model coordinates, normal to each measurement plane. Both the locations and the orientations of the measurement planes from the inboard camera are listed in Table 1.

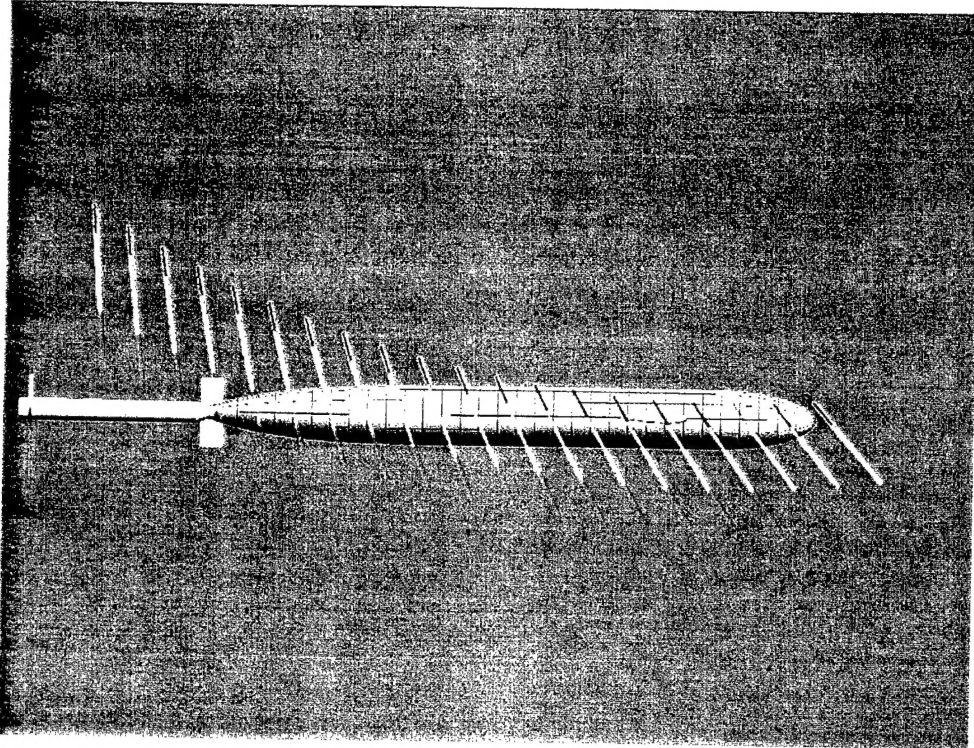


Fig. 1. Laser sheet position (data planes) relative to the model as it passes through the turn.

### PARTICLE IMAGE VELOCIMETRY (PIV)

Particle image velocimetry (PIV) is a flow-field measurement technique that provides an instantaneous distribution of two velocity components over an entire two-dimensional measurement plane. Fluid velocity is measured by tracking the mean motion of a group of small neutrally buoyant particles dispersed within the fluid, assuming that necessary care is taken to ensure that the particles faithfully track the flow. In a typical PIV implementation, the working fluid is seeded with microscopic tracer particles, and a selected plane of measurement is illuminated twice with a pulsed laser light sheet. The two exposures of the particle field are either recorded together in one double-exposed image or separately in two single-exposed frames. For PIV using double-exposed images, such as in present application, a means of shifting the second exposure from the first is used to eliminate the directional ambiguity arising from the inability to distinguish the sequence of exposure within a pair. During vector-map analysis, each image is subdivided into small interrogation windows. For each interrogation window of the double-exposed image, an auto-correlation function is calculated. The location of the peak of the correlation function represents the mean displacement of the tracer particles in each interrogation window. The average velocity in the window can then be readily calculated by dividing the mean particle displacement by  $\Delta t$ , the time separation between the two illumination pulses. Comprehensive reviews of PIV techniques may be found in the literature.<sup>5,6</sup>

Table 1. Locations ( $x_1$ ,  $y_1$ ,  $z_1$ ) and orientations ( $x_2$ ,  $y_2$ ,  $z_2$ ) of the inboard set of measurement planes, in model coordinates (ft). The left column represents the plane number, starting from the rightmost plane as shown in Figure 1.

Plane #	$x_1$	$y_1$	$z_1$	$x_2$	$y_2$	$z_2$
1	9.774	0.519	-0.348	-0.755	-0.656	-0.003
2	8.502	0.363	-0.387	-0.781	-0.624	-0.006
3	7.225	0.260	-0.428	-0.806	-0.592	-0.007
4	5.945	0.209	-0.471	-0.829	-0.559	-0.009
5	4.664	0.209	-0.516	-0.851	-0.525	-0.011
6	3.385	0.262	-0.562	-0.872	-0.49	-0.013
7	2.108	0.366	-0.611	-0.891	-0.454	-0.015
8	0.837	0.522	-0.660	-0.908	-0.418	-0.017
9	-0.427	0.730	-0.712	-0.925	-0.38	-0.019
10	-1.681	0.989	-0.765	-0.939	-0.342	-0.021
11	-2.923	1.299	-0.819	-0.952	-0.304	-0.023
12	-4.152	1.659	-0.874	-0.964	-0.265	-0.024
13	-5.365	2.068	-0.931	-0.974	-0.226	-0.026
14	-6.561	2.527	-0.989	-0.982	-0.186	-0.028
15	-7.737	3.033	-1.047	-0.989	-0.146	-0.029
16	-8.890	3.587	-1.107	-0.994	-0.106	-0.031
17	-10.021	4.188	-1.168	-0.997	-0.065	-0.033
18	-11.126	4.834	-1.229	-0.999	-0.025	-0.034
19	-12.204	5.525	-1.290	-0.999	0.016	-0.035
20	-13.253	6.258	-1.353	-0.998	0.056	-0.037

## EXPERIMENTAL SET-UP

### **ONR Body-1 Model and Sting**

The submarine model used in this study is Model 5484 with a length of 17.0 ft., a diameter of 1.55 ft. and configured as "ONR BODY-1." ONR BODY-1 is an unclassified generic submarine shape composed of an axisymmetric body, sail and 4 identical stern appendages. The sail has a NACA 0014 section with an aspect ratio of 0.27. It is faired to the hull and located at  $x/L = 0.2$ . The stern appendages, all identical in shape and size, are NACA 0018 foils with an aspect ratio of 1.2. A boundary layer trip wire, with an OD of 0.06 in., was mounted at  $x/L = 0.05$ . Particle injectors were also located just upstream of the trip wire (see Fig. 2). The injectors were not used while data were being recorded, but instead were used to seed the flow with particles before the start of a run.

The captive model is attached to the carriage using a sting mounting fixture; the assembly is shown dismounted from the carriage in Fig. 3a. A separate mounting fixture with struts is shown in the background of the figure but is not part of the sting. A line drawing giving greater detail of the sting arrangement is shown in Fig. 3b. The diameter of the sting is 6.5 in. except at the tailcone where it necks down to a 4 in. diameter for a distance of 9.25 in. then returns to the original diameter. The inside diameter of the tailcone is 5 in. at the point where the hull ends. The model was supported in an upright position (to allow easy access to the interior by removing the top covers) by two gimbals spaced 6 ft. apart. The gimbals were, in turn, mounted to a box beam located inside the model. With the cover removed from the top half of the model, one can see in Fig. 3a the tapered channel (box beam) affixed to the end of the sting. The sting was supported by an 8 in. diameter vertical cylinder with a length of 11.094 ft. between the pitch pivot and the hull centerline. The centerline of the vertical cylinder was 21.18 ft. aft of the forward perpendicular (FP). The model reference point, which corresponds to the longitudinal location of the center of buoyancy, was positioned on the hull centerline midway between the two gimbals, 7.7233 ft. aft of the forward perpendicular (FP).

The longitudinal, normal, and lateral force components with respect to the body axis were measured by means of three block-gage assemblies located at each gimbal. Pitching and yawing moments about the reference point were computed from the measured forces at each gimbal. The rolling moment about the longitudinal axis was measured by an additional gage located at the forward gimbal. The yaw and pitch angle of the model could be changed by yawing and pitching the entire sting assembly via the rotating arm undercarriage positioning equipment. The roll angle could be adjusted by rotating the model about the sting axis using roll positioning equipment built into the sting assembly. The roll angle was measured via a synchro-resolver located underwater inside the aft portion of the sting. Accelerometers calibrated to measure roll and pitch angle were installed in the model to allow for accurate zero settings. The nomenclature for the forces and moments is standard and may be found in the SNAME bulletin<sup>7</sup>; the positive directions for the forces and moments and the orientation of the coordinate system are given in Fig. 4. A cross-sectional view of a strut-mounted model attached to the rotating arm is given in Fig. 5.

In order to balance the static pitching moment of the sting assembly and model, the sting assembly was mounted to the rotating arm undercarriage in such a way that the model reference point was 7.000 ft. forward of the undercarriage pitch and yaw pivot point. As a result the radius to the model reference

point is altered as the model is pitched or yawed. For example, the yaw angle and radius at the model reference point is different than that set at the pivot point, as can be seen by the sketch in Fig. 6. The relationship between a yaw angle and radius at the undercarriage yaw pivot point ( $\psi_s$  and  $R_s$ , respectively), and yaw angle and radius at the model reference point ( $\psi_m$  and  $R_m$ , respectively), are as follows:

$$\psi_s = \psi_m + \sin^{-1} \left[ \frac{a \cos \psi_m}{R_s} \right] \quad (1)$$

$$\psi_m = \psi_s - \sin^{-1} \left[ \frac{a \cos \psi_s}{R_m} \right] \quad (2)$$

$$R_m = [R_s^2 + a^2 - 2a R_s \sin \psi_s]^{\frac{1}{2}} = R_s \frac{\cos \psi_s}{\cos \psi_m} \quad (3)$$

$$a = 11.094 \sin \theta + 7.000 \cos \theta, \quad (4)$$

where  $\theta$  is the model pitch angle.

### **Rotating Arm Basin**

The test was performed in the Rotating Arm Basin at NSWCCD. The Rotating Arm Basin is a circular basin, 260 feet in diameter and 20 feet deep. The rotating arm (a rotating bridge-like towing structure) pivots on a pedestal in the center of the basin and has a span of 129 ft and a width of 20 ft. (see Fig. 5). It is capable of towing a submarine or a surface-ship model in a circular path through calm water at a maximum linear speed of 30 knots in half a revolution at a radius of 120 ft. On the underside of the arm is an undercarriage which is movable and may be positioned radially to as many as 30 different radii. The previously described sting mounting fixture is attached to this undercarriage. Viewed from above, the arm rotates clockwise with steady angular velocity,  $r$ , and for a model mounted in the upright position, this implies that the model is executing a turn to starboard. The steady nondimensional yawing angular velocity,  $r'$ , is related to the length of the model,  $L$ , and the linear velocity  $U$  as follows:

$$r' = \frac{rL}{U}. \quad (5)$$

The linear velocity is, in turn, related to the angular velocity,  $r$ , and the towing radius,  $R$ , by

$$U = rR. \quad (6)$$

Therefore, the nondimensional angular velocity is typically expressed as

$$r' = \frac{L}{R} = \frac{1}{R'} \quad (7)$$

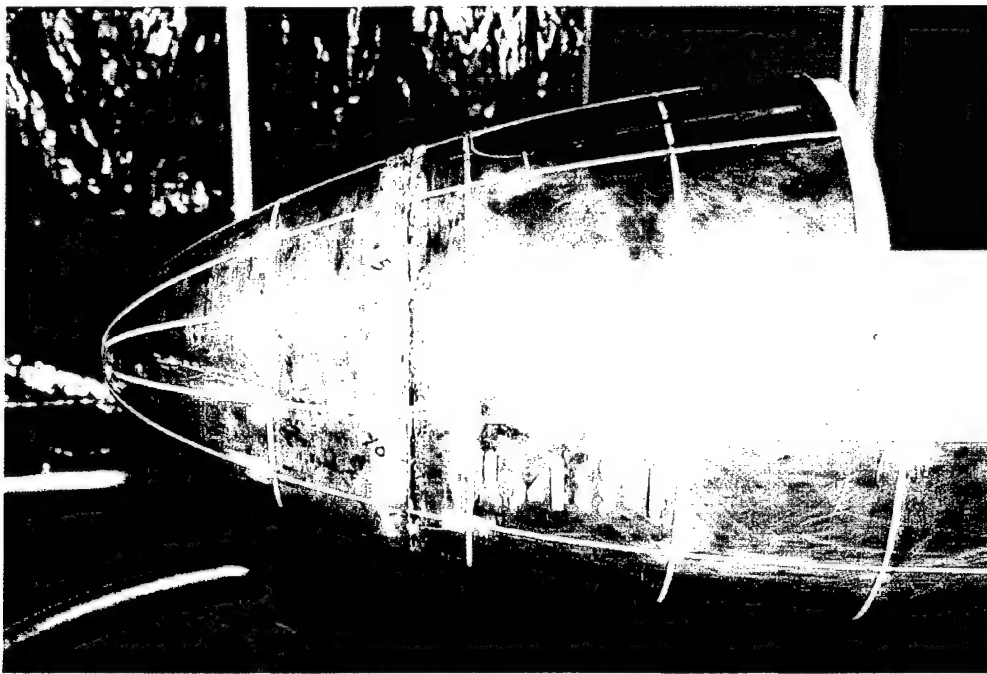


Fig. 2a. Profile view.

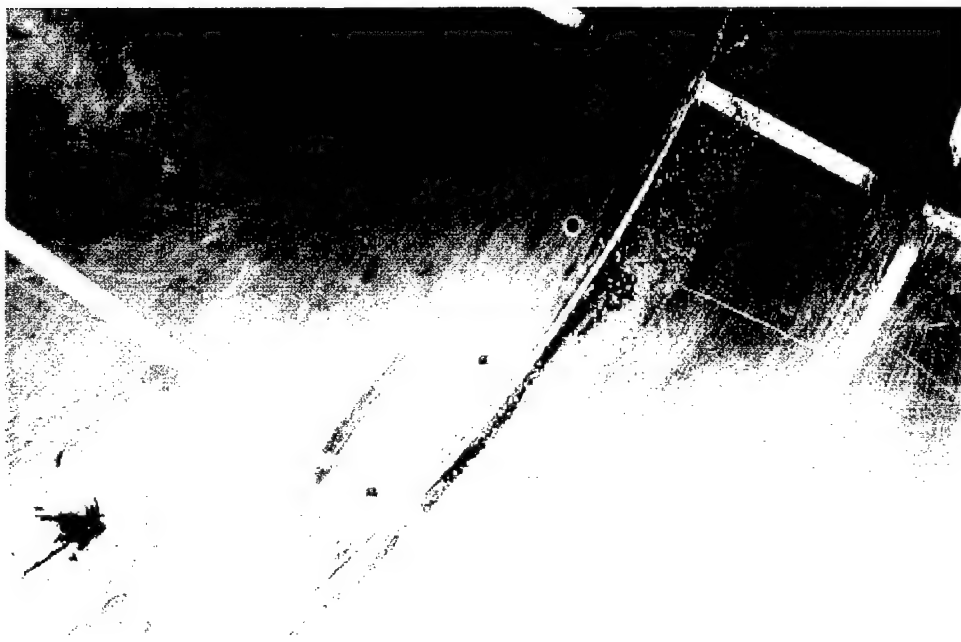


Fig. 2b. Close-up view.

Fig. 2. Dye injectors and boundary layer trip wire.

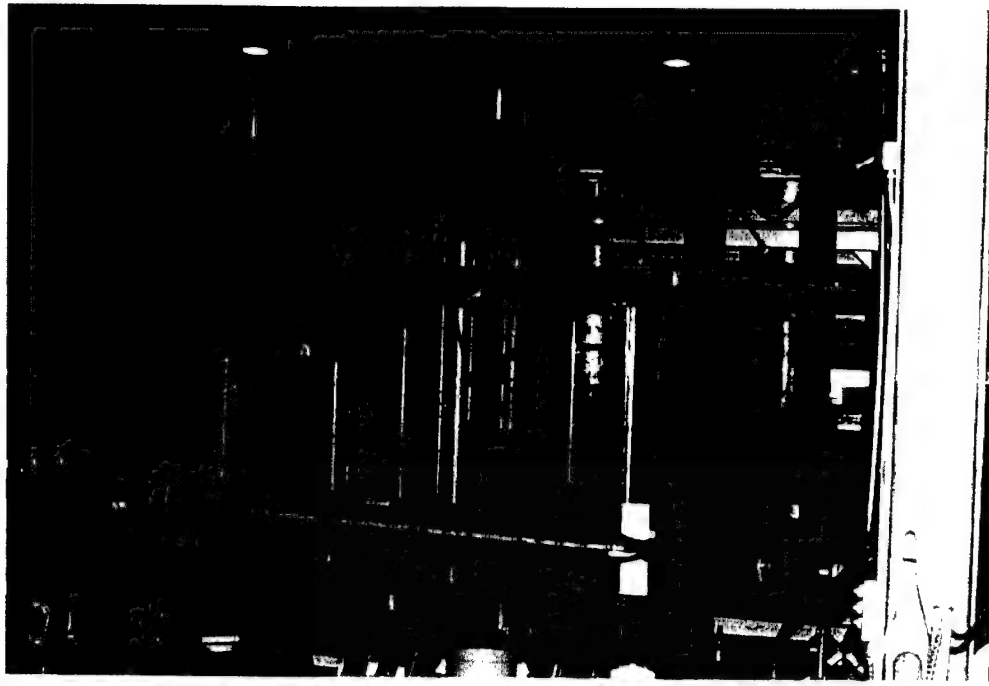


Fig. 3a. Sting mounted Model 5484, before connection to the carriage.

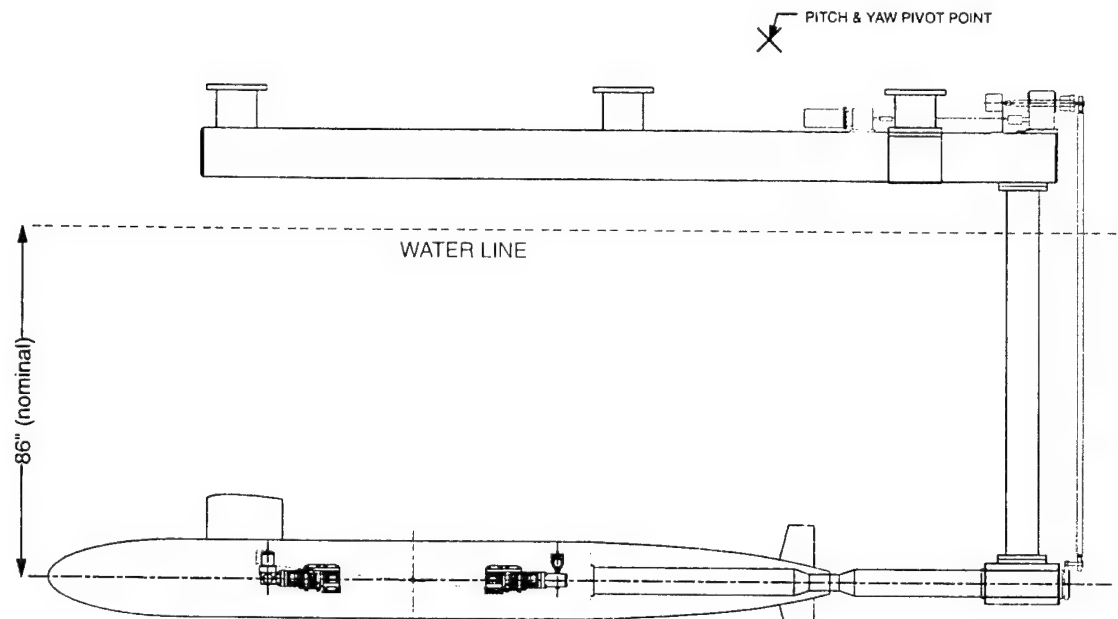


Fig. 3b. Line drawing.

Fig. 3. Sting-mounted Submarine for Rotating Arm Testing

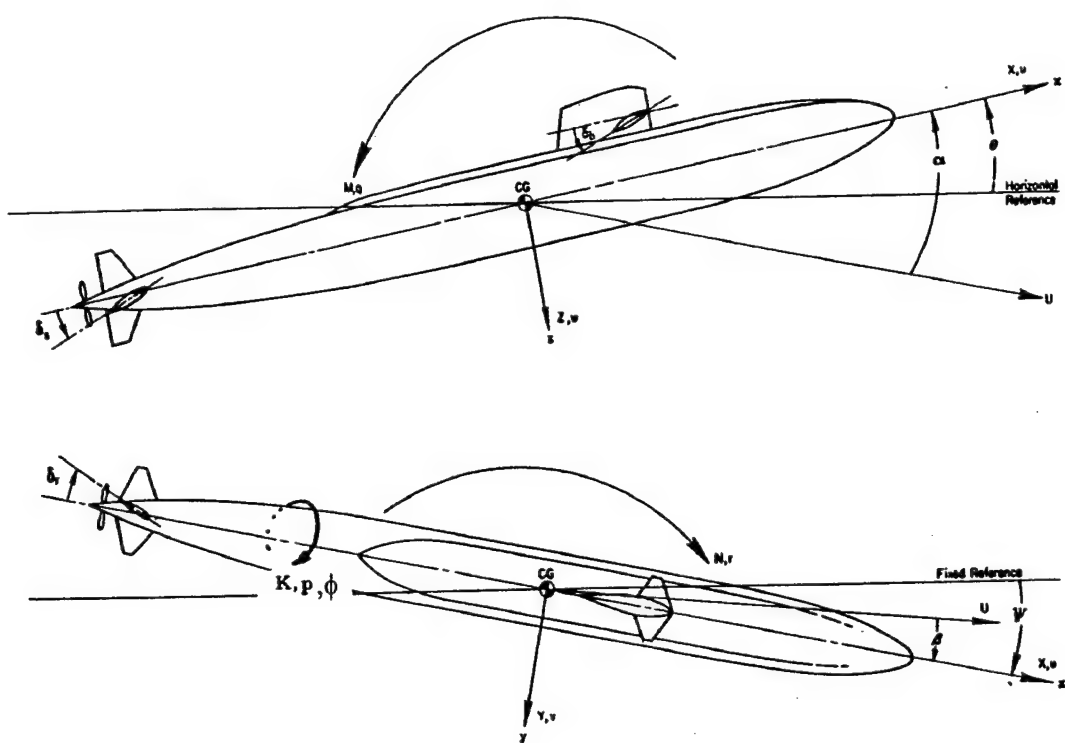


Fig. 4. Sketch showing standard submarine coordinate system and positive directions of angles, velocities, forces and moments.

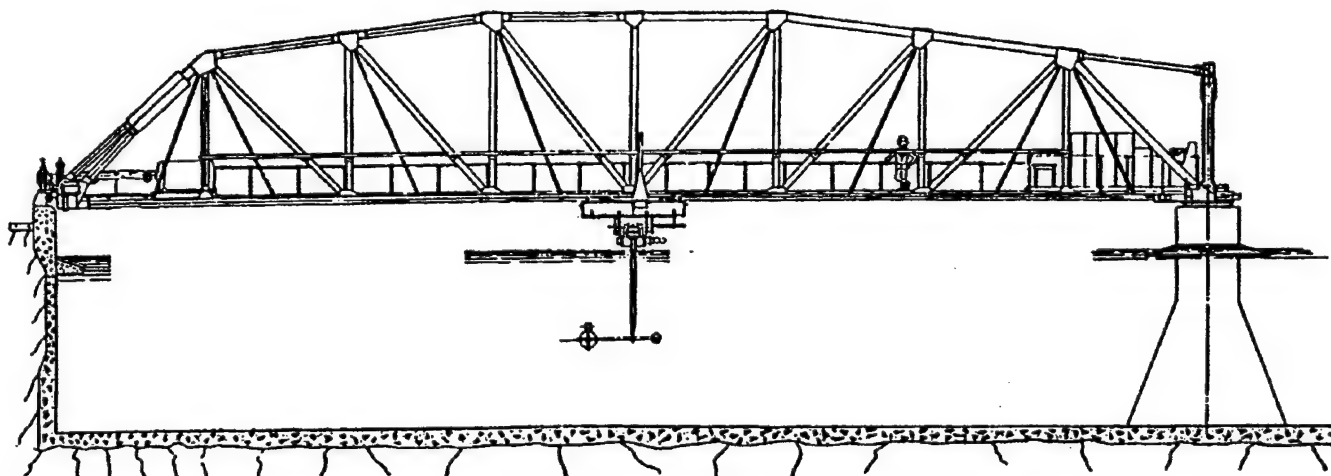


Fig. 5. Cross-sectional view of Rotating Arm facility.  
(Note that a strut-mounted submarine is depicted in this view.)

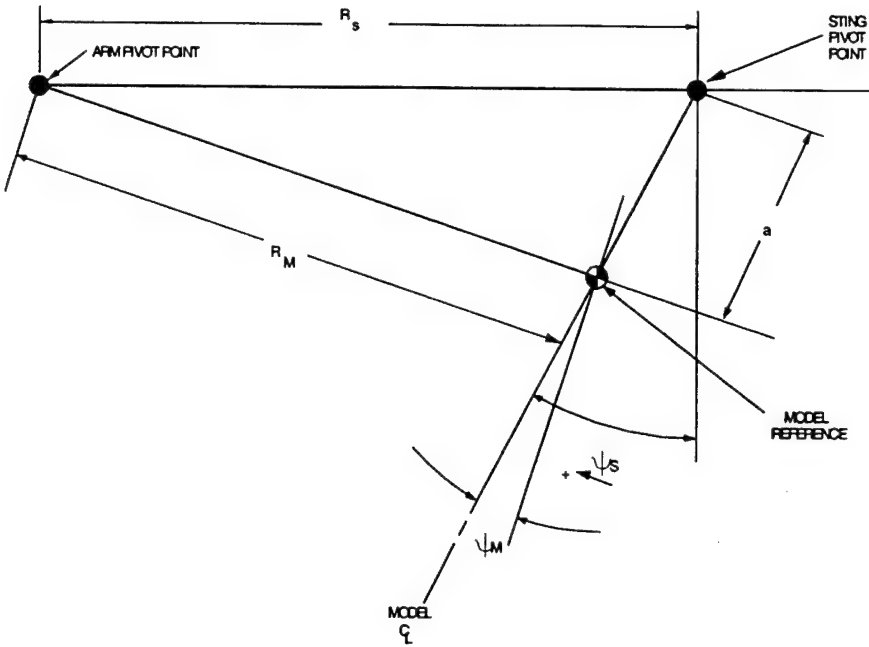


Fig. 6. Sketch showing relationships between yaw angles and radii.

### **Model Configuration**

In the present application, the ONR Body-1 model was mounted with a centerline depth of 6.67 ft. below the free-surface. The radius to the model reference point, ( $R_m$  in Fig. 6) was 32.206 ft., and the dimensionless radius was 1.89 after dividing by the model length of 17.0 ft. The angular velocity of the arm was  $r = 0.163$  rad/s. The linear speed at the model reference point was  $U = 5.26$  ft/s or 3.11 kn. Finally, the dimensionless angular velocity of the arm was found by inverting the dimensionless radius to get  $r' = 0.53$ . The model was oriented such that it was pitched at 2.0 deg (bow up), rolled 2.1 deg (to starboard) and yawed 9.5 deg to starboard ( $\psi_m$  in Fig. 6). The rudder was maintained at a fixed angle of -20 deg (for a starboard turn), and the sternplanes were set to -1.0 deg (rise). These configuration values were chosen as a result of conducting steady turning maneuvers with a free-running, radio-controlled model (RCM) configured as ONR Body-1. These values are representative of average conditions 32 sec after execution of the maneuvers during the steady portion of the turn.

Two configurations for testing were employed: with and without Micro Vortex Generators (MVGs). For both of these configurations, the model was oriented as described in the preceding paragraph. MVGs are constructed from 1/16 in aluminum angle and serve as passive flow control devices. The size of the MVGs (Size #6) is given by: 6.30 in long with a 1 in base and 0.9 in high. The MVGs were placed on the crown of the hull in alignment with the sail. Six MVGs were approximately evenly spaced in the axial direction with five placed downstream of the sail and one placed upstream as shown in Fig. 7. The precise locations relative to the forward perpendicular may be found in Table 2. For reference, the chord length of the sail is 22.489 in.

Fifty runs were acquired for Configuration 1 (No MVGs) followed by 20 runs for Configuration 2 (with MVGs). Then, the MVGs were removed and six additional runs with the model in Configuration 1 were obtained. Each run consisted of the following sequence of actions. The arm was accelerated from rest until the desired angular velocity of  $r = 0.163$  rad/s was reached (these conditions were maintained at steady state for approximately half of a revolution). The arm was by that time approximately 1/8 of a revolution from the center of the submerged PIV equipment. Force and moment data acquisition was then begun for a period of 10 s (approximately 1/4 of a revolution) at a rate of 100 Hz (for each channel of data). PIV data acquisition was started just prior to the bow of the model entering the field of view of the imaging equipment by means of a photo-interrupt trigger placed at a fixed location on the arm. PIV data acquisition continued until the desired 20 images taken at a rate of 4 Hz were obtained. The arm was then decelerated to rest. A minimum of 15-20 min were allowed to elapse between runs in order to allow the wake produced by the sting to subside.

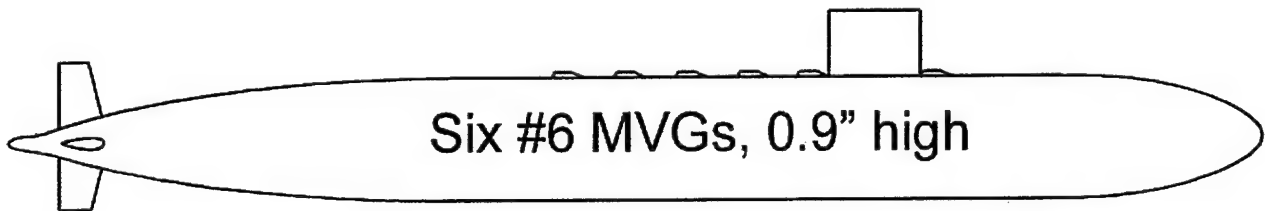


Fig. 7. Sketch showing MVG locations for Config. 2.

Table 2. Longitudinal distance from model FP to MVG TE.

MVG #	Distance ( $x/L$ )	Distance (ft)
1	0.1989	3.382
2	0.3401	5.781
3	0.3890	6.614
4	0.4381	7.447
5	0.4871	8.280
6	0.5361	9.114

### JHU Submersible PIV System

The measurement of the cross-flow velocity field around ONR Body-1 model was performed using the submersible PIV system from the Johns Hopkins University<sup>3</sup>. Schematics of the mechanical hardware, optics, and image acquisition and laser systems are presented in Figs. 8a, 8b, and 9. Two digital cameras, housed in their submersible enclosures, were used to image two adjacent areas (43cm x 43 cm

each) in a plane of measurement. Two sets of laser sheet optics in their housings were installed on a single optical rail to provide two possible measurement planes (although only one is used at a time). Light from a flashlamp-pumped dual-head dye laser, operating at an output of 120 mJ/pulse at 595 nm, was launched into a 400-micron fiber and expanded into a sheet to provide the required illumination. The camera housings and the laser sheet housings were mounted on a motor-driven turntable platform, which allowed adjustment of the orientation of the measurement system. The whole assembly then sat on top of a hydraulic scissors-jack, which permitted adjustment in the vertical position. The complete unit was lifted and placed within the Rotating Arm Basin. Fine adjustments in orientation and vertical position finally placed the cameras and laser sheet optics in the desired positions. Note that the pale blue lines visible in Figure 8 represent a chain drive and rail assembly mounted on the floor of the basin.

Each of the two image acquisition systems utilizes a scientific grade digital camera with a pixel resolution of 2K x 2K (model 4m4, Silicon Mountain Design, Inc.). The camera contains a high-performance 28.7mm x 28.7mm CCD array and is capable of capturing 12-bit images at a frame rate of 4 fps. The camera, thus, has a maximum output of 24 Mb/s in RS422 data format. One inherent limitation of the RS422 data format is that the data integrity degrades significantly for cable lengths of more than 100 ft. To overcome this limitation, the data is first converted into MECL (Motorola emitter-coupled logic) format before it is transmitted through the required 250-ft. cable length necessary for the experiment. At the other end, the data is then converted back to RS422 before being recorded by the host computer. To manage such a large data rate (24 Mb/s) the data stream was recorded in real time onto an array of hard disks controlled by a Boulder Instruments, Inc. (model Streamstor PCI-306) disk array controller. This "real-time disk" system allows the image acquisition system to capture as much as 80 GB of images continuously at the full frame rate of the camera.

A schematic of the image-forming lens system is shown in Fig. 10. The desired wide coverage (43cm x 43cm) dictates the usage of a wide-angle lens in order to minimize the subject to lens distance. Reducing the amount of water between the subject and the lens results in sharper detail and increased contrast. To compensate for the distortions introduced by the refraction at the water/optical-window/air interface at the front of the housing, a concentric spherical dome port is used instead of a flat optical window. When a dome port is used between water and air, it acts as a diverging (negative) lens. The optics of the diverging lens results in a virtual image being formed a short distance in front of the dome port. To make it possible to focus on the virtual image, the 28mm photographic lens is fitted with a multi-element,+2 diopter, close-up lens. For wide-angle underwater application, the image-forming lens system results in extremely flat-field imaging, yielding only a 2% maximum distortion around the edges.

Raw images of double-exposed particles were processed into velocity data using a PIV analysis software package from LaVision, Inc. The DaVis software package utilizes advanced algorithms, including local adaptive cell shift and second-order correlation, to enhance accuracy and improve data integrity. A benchmarking test was carried out to measure the stability and accuracy of the software package against a set of "standard" images provided by the PIV-STD project. The PIV-STD project was developed to provide standards and guide tools for the PIV community (the project website can be found at <http://vsj.or.jp/piv/>). One useful product of this project was a set of computer-generated standard PIV images that a PIV practitioner can use to benchmark his or her analysis algorithms. The benchmarking

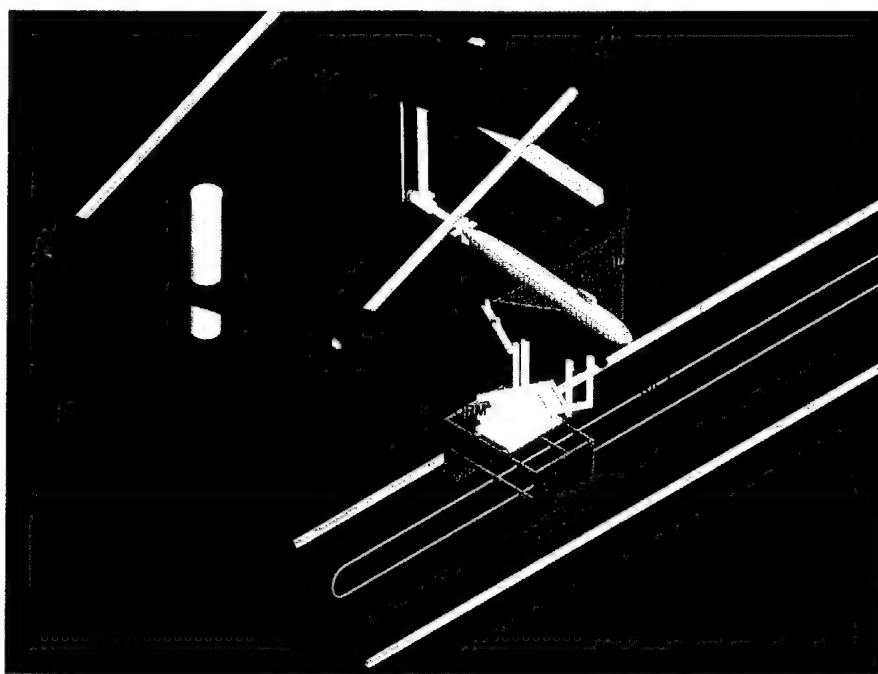


Fig. 8a. Overview

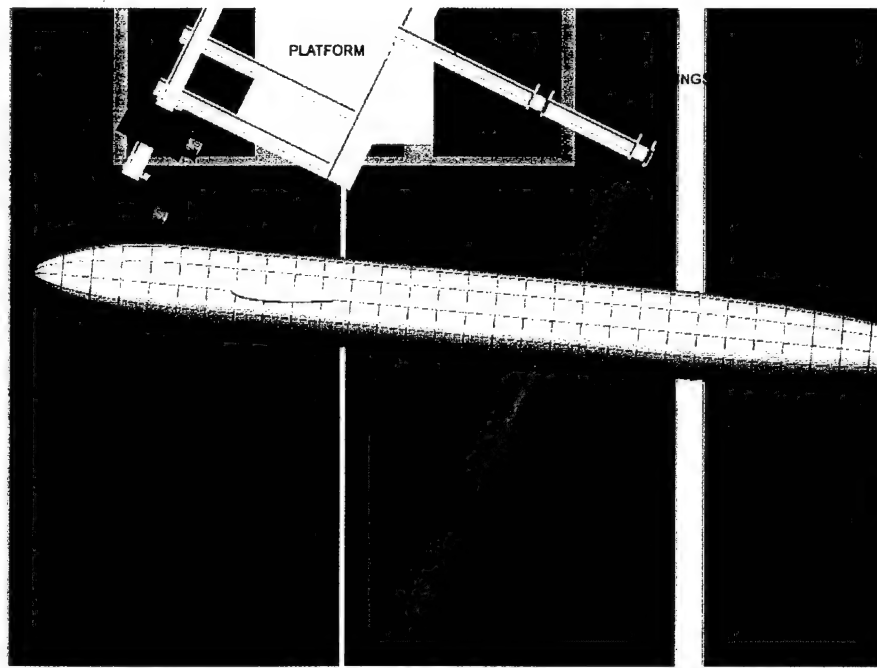


Fig. 8b. Close-up view.

Fig. 8. Submerged PIV instrumentation deployed in the Rotating Arm Basin.

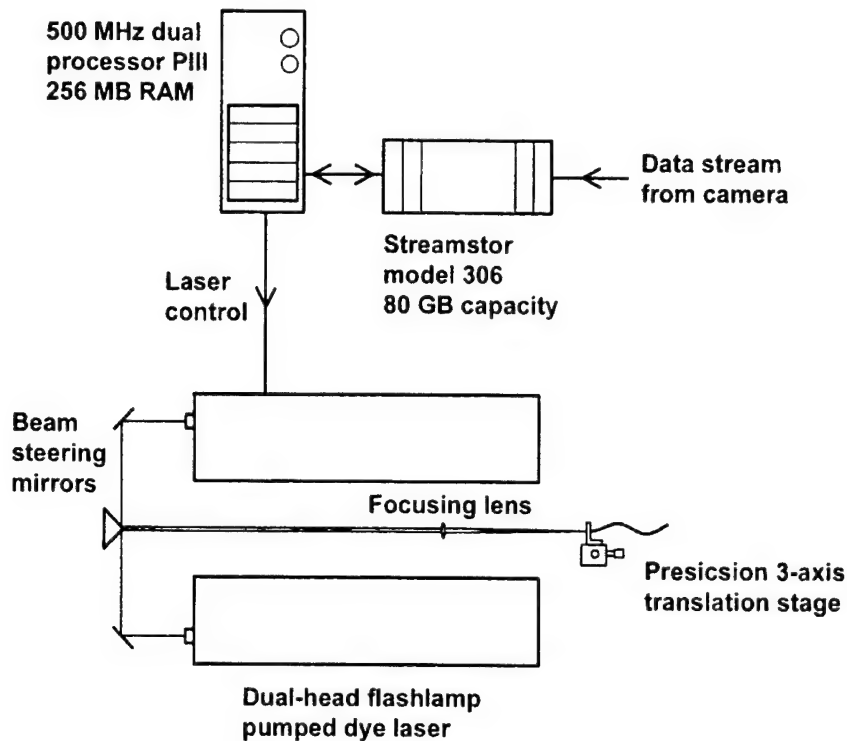


Fig. 9. PIV instrumentation: image acquisition and laser systems.

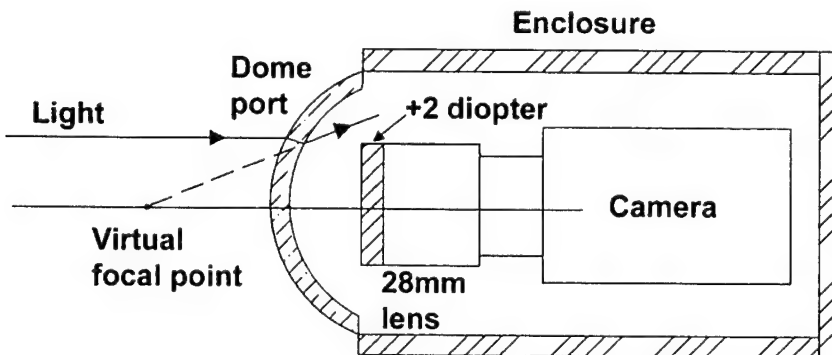


Fig. 10. Camera lens optics and submersible enclosure.

test showed that the DaVis software package compares very well with other state-of-the-art analysis software packages, providing a high degree of stability, accuracy, and user-friendliness.

One of the critical issues in utilizing PIV is the importance of providing a uniform distribution of PIV particles in the image plane. For this test, this issue was a particular concern due to the large volume of fluid that needs to be seeded. The model itself was used as the seeding device by utilizing injector ports on the nose of the model. Approximately 30 gallons of a dilute mixture (1500 ppm) of 15-micron

hollow glass spheres and water was pumped to the injectors through a plenum and a network of Tygon tubing to seed the flow. This process not only guaranteed that there were enough seed particles around the model but also that the particles were placed at the correct depth. Seeding of the flow field was done initially at the start of each day. Re-seeding after every third run was found to be necessary due to dispersion of the particles throughout the tank.

## FORCE AND MOMENT MEASUREMENTS

A forward and an aft set of block gages were used to measure the longitudinal, lateral and vertical force components with respect to the body axes, denoted  $X$ ,  $Y$  and  $Z$ , respectively. The forward and the aft set of block gages was attached to a tapered channel inside the model through two gimbals. The longitudinal distance between the centerline of the two gimbals was 6 feet. The origin of the body coordinate system or reference point was located 7.723 ft aft of the forward perpendicular along the centerline of the hull. The pitching and yawing moments about the reference point,  $M$  and  $N$ , were determined from the difference in the measured reaction forces at each gimbal, multiplied by one-half the spacing between the two gimbals. The roll moment,  $K$ , was measured by a strain gage unit located at the forward strut.

Before a run is made, small nonzero forces and moments present at each gage (electrical zeros) are measured and recorded so that they can be removed from the underway force and moment data. The underway force and moment data were then non-dimensionalized. Representative equations for vertical force,  $Z'_T$ , and pitching moment,  $M'_T$ , are shown in Eq. 8, and similar equations apply for the remaining quantities,

$$Z'_T = \frac{(Z_1 + Z_2) - (Z_1 + Z_2)_0}{\frac{1}{2} \rho U^2 L^2} \quad \text{and} \quad M'_T = \frac{[(Z_2 - Z_1) - (Z_2 - Z_1)_0] L_h}{\frac{1}{2} \rho U^2 L^3}, \quad (8)$$

where  $Z_1$  and  $Z_2$  are the vertical force measurements from the forward and aft block gages, respectively. The subscript "0" indicates the values of the electrical zeros, and the prime symbol denotes dimensionless values. The density value that was used in the normalization was 1.9367 slugs/ft<sup>3</sup>.

During a run, the measurements of each force and moment include both a contribution due to the hydrodynamic force distributions over the hull and appendages and a contribution due to the acceleration of the mass of the model. The latter contribution was removed from the measurements to determine the hydrodynamic forces and moments by using the equations shown in Table 2 with the values of the constants from Table 3. The notation for the dimensionless linear velocities:  $u'$ ,  $v'$  and  $w'$ , and the dimensionless angular velocities:  $p'$ ,  $q'$  and  $r'$ , is standard and is defined in the SNAME reference<sup>7</sup>.

Each of the instantaneous values in the time series for each of the force and moment variables had tares removed and were rendered dimensionless in the manner described above. The data were then averaged over the 10.0 s sampling period of the measurements for each run. The mean values for each run were then averaged over the 50 runs acquired for Configuration 1 without MVGs. These data are shown in

Table 4. Similarly, mean values for each of the 20 runs of Configuration 2 with MVGs were averaged to produce the data shown in Table 5. Also shown in Tables 4 and 5 are standard deviations of the mean values computed across the 50 runs and 20 runs, respectively. Sample means and standard deviations were computed using the standard formulas:

$$\bar{X} = \frac{1}{N} \sum_{i=1}^N X_i \quad \text{and} \quad S_x = \left[ \frac{1}{N-1} \sum_{i=1}^N (X_i - \bar{X})^2 \right]^{\frac{1}{2}}, \quad (9)$$

where  $N$  is the number of runs in Config. 1 and Config. 2, respectively.

Following Coleman and Steele<sup>8</sup>, a precision index for a variable  $X$  and for its mean value  $\bar{X}$  may be computed using

$$P_x = t S_x \quad \text{and} \quad P_{\bar{X}} = t S_{\bar{X}} = \frac{t S_x}{\sqrt{N}}, \quad (10)$$

where  $t$  is a value drawn from Student's  $t$ -distribution for  $N-1$  degrees of freedom and a specified confidence level. Note that the normalized variable  $(X - \mu)/S_x$ , where  $\mu$  is the true mean value of the parent distribution from which only a sample of  $N$  measurements was drawn, is not normally distributed but instead is distributed according to Student's  $t$ -distribution and is the reason for its use in Eq. 10. The  $t$ -values for  $N-1=19$  and  $N-1=49$  and for a confidence level of 0.95 are 2.093 and 2.010, respectively. After computing the precision indices, we can then determine 95% confidence intervals for the true mean value of the parent distribution as described by

$$\text{Prob} (\bar{X} - P_{\bar{X}} \leq \mu \leq \bar{X} + P_{\bar{X}}) = 0.95. \quad (11)$$

The 95% confidence bounds  $\bar{X} - P_{\bar{X}}$  and  $\bar{X} + P_{\bar{X}}$  are also supplied in Tables 4 and 5. Tables 6 and 7 give similar quantities for force and moment variables returned to dimensional form.

Before proceeding further, some comments are in order to describe how one should apply Eq. 10 to compute precision indices. Assume for the moment that only a single run was available for the computation of mean values of the forces and moments. A total of 1000 measurements, 100 per second for 10 s, were acquired for each of the forces and moments during the run. Should  $N$  equal 1000 for the computation of  $P_{\bar{X}}$ ? Implicit in the definition of Eq. 10 is the fact that the  $N$  instantaneous values must be *independent* measurements of  $X$ . Therefore, one must determine the smallest timescale over which the variable  $X$  can change. Successive measurements of  $X$  that are separated by a time less than this inherent timescale are not independent measurements. To determine this timescale, one may compute a power spectrum of  $X$  and determine the largest frequency at which there is any noticeable power (that is not due to noise) in the signal. The data would suggest that this cutoff is somewhere in the 6-10 Hz range, a conservative estimate being 5 Hz. Therefore, only 5 samples per second are independent, and  $N = 50$  for the 10 s sample period. If only one run existed, then using this value of  $N$  would be justified and would provide a more realistic estimate of the precision index of the mean than by using  $N = 1000$ .

Now, return to the fact that we have 50 runs for configuration 1 and 20 runs for configuration 2. Assume that an additional source of precision uncertainty is present – random errors that arise run-to-run. If only one run were available, then the precision index computed as described in the previous paragraph would contain no information about run-to-run uncertainty, yet it would be the best that we could do. The fact that we have multiple runs, however, gives us an opportunity to compute a more realistic estimate of the precision index of the mean that includes run-to-run uncertainty. This means that even though a mean value computed for each run is the result of many *independent*, instantaneous measurements, these multiple measurements within a given run give us no information about any run-to-run variation in the data. Thus, we use the mean value for each run to form a mean value for each configuration, and we assess the precision error using  $N = 50$  for Config. 1 and  $N = 20$  for Config. 2.

The procedure, then, was as follows. A simple mean value for each of the forces and moments was computed (using Eq. 9) from the instantaneous measurements from each run using  $N = 1000$ . A set of 50 mean values for Config. 1 and 20 mean values for Config. 2 were then obtained for each variable. Then, a final mean value and standard deviation was computed for each variable for Config. 1 and Config. 2 using  $N = 50$  and  $N = 20$ , respectively. The precision index of the mean was then computed using Eq. 10 with  $N = 50$  and  $N = 20$ , respectively.

Examining Table 6 one can see that the fluid exerts on the model without MVGs a steady drag of 8.51 lbs, a force to starboard (into the turn) of 40.87 lbs and a very small upward force of 1.16 lbs. The latter value is not unreasonable given the 2 deg bow-up pitch of the model. The drag and spanwise forces are steady with standard deviations less than 4%. The model experiences a rolling moment to starboard of 4.99 ft lbs which results from the fact that the fluid exerts a force component on the sail, which is asymmetric about the centerline. The fluid appears to exert a small pitch-down moment on the model of 0.66 lbs, but this is statistically insignificant due to the large standard deviation. Finally, with a yaw angle of 9.5 deg to starboard, the model experiences small drift angles at the bow and much larger drift angles at the stern during clockwise rotation with angular velocity  $r$ . As a result, the fluid exerts a steady moment of 19.62 ft-lbs in the counter-clockwise direction.

The MVGs are designed to have a minimal contribution to the drag component, and this is borne out by examination of  $\bar{X}$  in Tables 7 and 8. In fact, there appears to be a small reduction in drag with MVGs present; however, the change is only slightly larger than the standard deviation and is likely not significant. Small increases in spanwise force and rolling and yawing moments may be the net result of additional forces exerted on the raised portions of the MVGs. The most obvious changes are the moderate downward vertical force of 8.22 lbs and the very large bow-up pitch moment of 59.10 1bs. The large pitch-up moment is consistent with behavior observed previously. Namely, 688-class submarines display a tendency to pitch down and, as a result, increase depth during moderate to high-speed turns. MVGs mounted on a 688-class radio-controlled free-running model (RCM) in the configuration shown in Fig. 7 were able to significantly reduce the initial severe pitch-down tendency, and were able to reduce pitch and depth loss throughout the steady portion of the turning maneuver<sup>1</sup>. One of the goals of this study is to learn from the PIV measurements the manner in which the MVGs modify the complex three-dimensional flow field about the hull to produce the large pitch-up moment.

Table 3. Equations to determine hydrodynamic coefficients from measured coefficients for rotating arm sting experiments

$$X' = X_T' + B_1(w'q' - v'r') - B_1B_5(q'^2 + r'^2) + B_1B_6p'q' + B_1B_7p'r'$$

$$Y' = Y_T' + B_2(u'r' - w'p') + B_2B_5q'p' - B_2B_6(r'^2 + p'^2) + B_2B_7q'r'$$

$$Z' = Z_T' + B_3(v'p' - u'q') + B_3B_5r'p' + B_3B_6r'q' - B_3B_7(p'^2 + q'^2)$$

$$K' = K'_T + B_4B_6(v'p' - u'q') + B_4B_7(w'p' - u'r') + (B_{10} - B_9)q'r' + B_{11}p'r' + B_{12}(r'^2 - q'^2) - B_{13}p'q'$$

$$N' = N'_T + B_2B_5(u'r' - w'p') + B_2B_6(v'r' - w'q') + (B_9 - B_8)q'p' + B_{11}(q'^2 - p'^2) - B_{12}r'p' + B_{13}r'q'$$

$$M' = M'_T + B_3B_5(u'q' - v'p') + B_3B_7(w'q' - v'r') + (B_8 - B_{10})r'p' - B_{11}q'r' + B_{12}q'p' + B_{13}(p'^2 - r'^2)$$

where the subscript T in the equations denotes total forces or moments as measured by the gages and:

$B_1 = m_x'$  (  $m'$  as seen by the x gage )

$B_2 = m_y'$  (  $m'$  as seen by the y gage )

$B_3 = m_z'$  (  $m'$  as seen by the z gage )

$B_4 = m_k'$  (  $m'$  as seen by the k gage )

$B_5 = x_G'$  (  $x'$  distance from reference to model center of gravity )

$B_6 = y_G'$  (  $y'$  distance from reference to model center of gravity )

$B_7 = z_G'$  (  $z'$  distance from reference to model center of gravity )

$B_8 = I_x'$  ( nondimensional Moment of Inertia about x axis )

$B_9 = I_y'$  ( nondimensional Moment of Inertia about y axis )

$B_{10} = I_z'$  ( nondimensional Moment of Inertia about z axis )

$B_{11} = I_{XY}'$  ( nondimensional Product of Inertia with respect to x and y axes )

$B_{12} = I_{YZ}'$  ( nondimensional Product of Inertia with respect to y and z axes )

$B_{13} = I_{ZX}'$  ( nondimensional Product of Inertia with respect to z and x axes )

Table 4. Constants to be used in the equations shown in Table 2.

Coefficient	Definition	Value
B <sub>1</sub>	m <sub>x</sub>	0.011102
B <sub>2</sub>	m <sub>y</sub>	0.011334
B <sub>3</sub>	m <sub>z</sub>	0.011607
B <sub>4</sub>	m <sub>k</sub>	0.011751
B <sub>5</sub>	x <sub>G</sub>	-0.005892
B <sub>6</sub>	y <sub>G</sub>	0.0
B <sub>7</sub>	z <sub>G</sub>	-0.000439
B <sub>8</sub>	I <sub>x</sub>	0.00001004
B <sub>9</sub>	I <sub>y</sub>	0.0005904
B <sub>10</sub>	I <sub>z</sub>	0.0005904
B <sub>11</sub>	I <sub>xy</sub>	0.0
B <sub>12</sub>	I <sub>yz</sub>	0.0
B <sub>13</sub>	I <sub>zx</sub>	0.0

Table 5. Dimensionless Force and Moment Measurements for Config. 1

	X'×10 <sup>3</sup>	Y'×10 <sup>3</sup>	Z'×10 <sup>3</sup>	K'×10 <sup>5</sup>	M'×10 <sup>5</sup>	N'×10 <sup>5</sup>
Mean	-1.10	5.29	-0.15	3.80	-0.50	-14.95
Std. Dev.	0.04	0.14	0.07	0.37	1.76	1.03
$\bar{F}' - P_{\bar{F}}$	-1.11	5.25	-0.17	3.69	-1.00	-15.24
$\bar{F}' + P_{\bar{F}}$	-1.09	5.33	-0.13	3.91	0.00	-14.65

Table 6. Dimensionless Force and Moment Measurements for Config. 2

	X'×10 <sup>3</sup>	Y'×10 <sup>3</sup>	Z'×10 <sup>3</sup>	K'×10 <sup>5</sup>	M'×10 <sup>5</sup>	N'×10 <sup>5</sup>
Mean	-1.05	5.54	1.07	4.41	45.23	-16.42
Std. Dev.	0.04	0.12	0.11	0.77	4.33	1.10
$\bar{F}' - P_{\bar{F}}$	-1.07	5.48	1.02	4.05	43.20	-16.94
$\bar{F}' + P_{\bar{F}}$	-1.03	5.60	1.12	4.77	47.25	-15.91

Table 7. Dimensional Force and Moment Measurements for Config. 1  
in *lbs* and *ft-lbs*, respectively

	X	Y	Z	K	M	N
Mean	-8.51	40.87	-1.16	4.99	-0.66	-19.62
Std. Dev.	0.32	1.08	0.51	0.49	2.31	1.37
$\bar{F} - P_{\bar{F}}$	-8.60	40.56	-1.31	4.85	-1.32	-20.01
$\bar{F} + P_{\bar{F}}$	-8.42	41.18	-1.02	5.13	-0.004	-19.23

Table 8. Dimensional Force and Moment Measurements for Config. 2  
in *lbs* and *ft-lbs*, respectively

	X	Y	Z	K	M	N
Mean	-8.06	42.59	8.22	5.77	59.10	-21.46
Std. Dev.	0.31	0.93	0.85	1.00	5.65	1.44
$\bar{F} - P_{\bar{F}}$	-8.21	42.16	7.83	5.30	56.45	-22.14
$\bar{F} + P_{\bar{F}}$	-7.92	43.03	8.62	6.23	61.74	-20.79

## RESULTS AND DISCUSSION

The purpose of Part I of this paper is to provide the reader with the details of the experimental arrangements and a short discussion of the relevant flow phenomenology. A more detailed presentation of the PIV data, along with the force and moment measurements, will yield a more complete discussion in Part II of the paper.

The maneuvering characteristics of a submarine depend on the hydrodynamic forces and moments that are developed on the hull, appendages, and propeller. In a turning maneuver the lift that is developed on the deflected rudder causes the submarine to develop yawing angular velocity and an angle of drift,  $\beta$  (defined in Figure 4), resulting in the submarine pointing into the turn. The combination of the yawing angular velocity and forward motion of the vehicle produces a variation of the angle of drift over the entire length of the submarine. At a point just ahead of the sail, the local angle of drift is zero. From that point aft, the angle of drift increases so that at the rudder, the local angle of drift is quite large. As lift is developed from the sail, a strong vortex is shed from near the tip, and is convected downstream with the ahead speed of the submarine. The lift on the sail also causes a large transient rolling angular velocity and large roll angle. This snaproll is the initial peak in the roll angle response, and it is usually much larger than the steady roll angle. The data presented in this paper is for the ONR Body-1 in a steady turn, pitched at 2.0 deg (bow up), rolled 2.1 deg (to starboard), and yawed 9.5 deg (to starboard). The rudder was maintained at a fixed angle of -20 deg (for a starboard turn), and the sternplanes were set to -1.0 deg (rise). These configuration values were chosen as a result of conducting steady turning maneuvers with a free-running, radio-controlled model (RCM), configured as ONR Body-1. These values are representative of average conditions 32 sec after execution of the maneuvers during the steady portion of the turn.

Figure 11 shows an example of the velocity (represented by vectors) and vorticity fields (represented by contours) in a cross plane, downstream of the sail, looking aft for Configuration 1 (without MVGs). The plane of measurement is the tenth plane from the nose of the model as shown in Figure 1. The thick-lined curve represents the location on the submarine body where the laser sheet hits the model. The area between the thick-lined curve and the thin-lined curve (in gray) represents the area contaminated by the bright diffuse reflection off the body, rendering data in that region unreliable. Table 7 lists dimensional forces and moments on the model for Configuration 1. Of relevance to current discussion are the average vertical force,  $Z$ , with a value of -1.16 lbs (upward) and the average pitching moment,  $M$ , with a value of -0.66 ft-lbs (pitch down).

Evident in the measured flow field and vorticity contours is a prominent trailing vortex around  $y = 1.2$  ft. and  $z = -1.1$  ft., which originated from the tip of the sail of the model undergoing a steady turn. At the instance of measurement, the model heading is approximately out of the page, with the sail mounted on top. Because the model is undergoing a mildly severe turn with  $r' = 0.53$  and is pitched up slightly and yawed to starboard, the local angle of drift and cross flow velocity geometrically dictates that a region of flow separation is expected on the leeward side of the body, slightly towards the deck. The velocity and vorticity field in Figure 11 show a region of negative vorticity around  $y = 1.1$  ft. and  $z = -0.2$  ft., being shed in the starboard area, and a region of positive vorticity (CCW, partially out of view) on the deck of the model ( $z = -0.8$  ft.). These two regions represent points of flow separation commonly observed

around a bluff body in a cross flow; however, they appear to be rotated clockwise from what is normally expected, judging from the direction of local angle of drift and cross flow velocity alone. The region between the two separation points is normally a region of low vorticity, as observed in Figure 11.

An argument is presented here that the sail tip vortex, due to its strength and proximity to the body, will tend to delay the starboard separation and enhance the deck separation by effectively imposing a negative circulation (CW) around the body. In other words, the interaction of the sail trailing vortex with the body will generate a negative vorticity flux across the body such that the separation points will rotate clockwise, as observed in Figure 11. Because the separation zone is an area of low pressure (with a corresponding area of high pressure on the opposite side of the hull), the aforementioned mechanism which causes the low pressure region to rotate towards the deck, contributes to an upward force on the hull aft of the sail. Since the trailing vortex originates around the tip of the sail and the CG on the ONR Body-1 model is situated close to (0.145L aft) the trailing edge of the sail, the interaction of the sail tip vortex with the hull exerts most of the influence aft of the CG. An upward force which acts primarily aft of the CG will result in a net downward pitching moment, consistent with the measured results.

It is important to note that the mechanisms leading to the downward pitching moment discussed above are limited to situations in which cross-flow separation is dominant, i.e., a submarine in a turn with large  $r'$ . In fact, a submarine with a similar body/sail configuration has been observed to pitch up in a mild turn. A more detailed discussion of this point, with relevant observations from existing literature, will be deferred to Part II of the paper.

Figure 12 shows a comparable flow field as compared to Figure 11, but in this case the submarine model is fitted with MVGs (Configuration 2) as shown in Figure 7. For this case (see Table 8), the average vertical force,  $Z$ , was measured to be 8.22 lbs (downward), and the average dimensionless pitching moment,  $M$ , has a value of 59.10 ft-lbs (pitch up). Note that MVGs contribute significantly to a downward vertical force and an upward pitching moment. This net downward vertical force and upward pitching moment can be explained in terms of the flow field observed in Figure 12. Evident in Figure 12 is the existence of a prominent large-scale vortical structure with counter-clockwise (positive) circulation around the deck of the model. This region of high vorticity is likely the result of tip vortices shed from the MVGs themselves. The tip vortices from each MVG section are like-signed and would tend to roll-up into a larger single vortical structure. Because this vortex is very near the body, it serves to bring high momentum fluid into this region of normally low pressure and will effectively reattach the boundary layer, working much like MVGs on an aircraft wing. This delay of flow separation on the deck in the aft section will in effect result in a pressure recovery, netting the model a downward vertical force aft of the sail and a corresponding positive pitch-up moment. Taking the difference in the average vertical force,  $Z$ , and the average pitching moment,  $M$ , between Configuration 2 (MVGs) and Configuration 1 (no MVG) yields a value of 9.38 lbs (net downward vertical force) and 59.76 ft-lbs (net pitch up moment), respectively. The measured vertical forces and moments and the differences thereof between Configuration 1 and 2 are consistent with the observed flow field and the proposed mechanism of interaction between the sail trailing vortex and the hull separated flow.

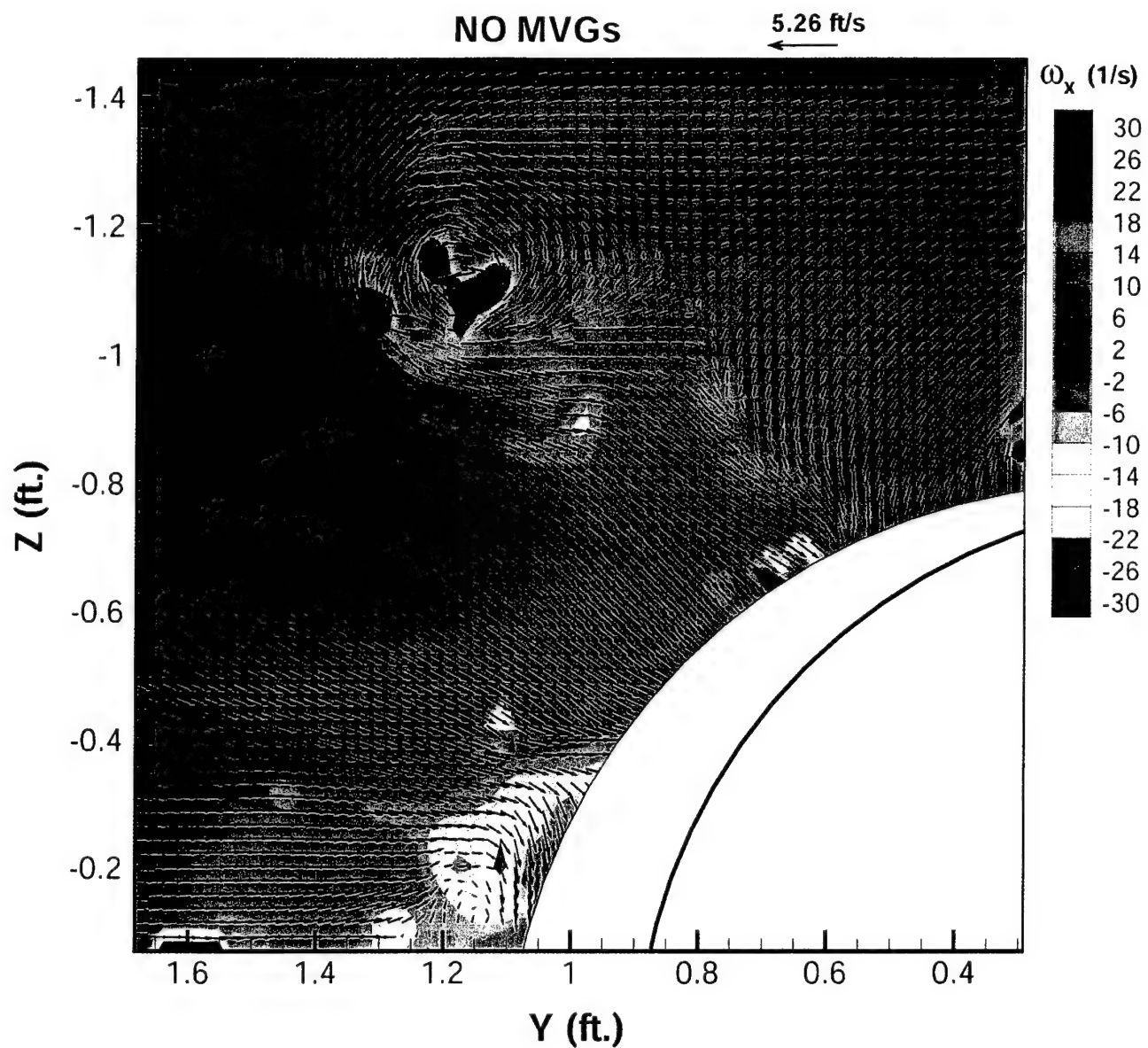


Fig. 11. Cross-cut velocity and vorticity field, no MVGs.

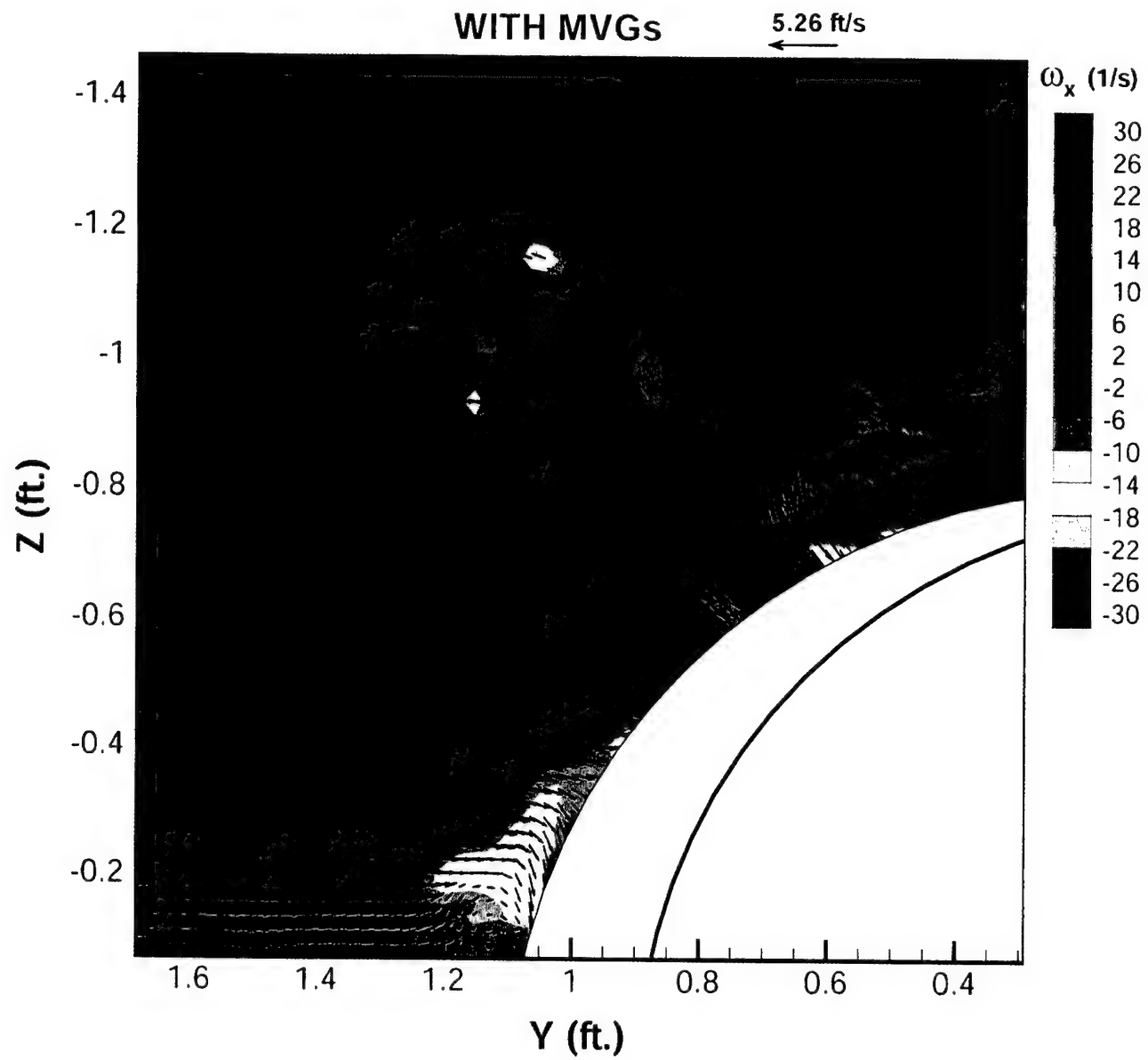


Fig. 12. Cross-cut velocity and vorticity field, with MVGs.

As discussed in a previous section, the various parameters defining the orientation of the vehicle for captive model testing were taken from conditions developed on a free-running, radio-controlled model (RCM). Specifically, the RCM conducted a series of turning maneuvers, and the configuration parameters are representative of average conditions 32 sec after execution of the maneuvers during the steady portion of the turn. This captive model experiment provides insight into the hydrodynamic conditions that prevail during that steady turning phase. However, during a free-running maneuver, the submarine transitions from steady forward motion to the steady turning phase in a period of time dominated by unsteady effects.

This unsteady phase of the free-running maneuver begins with the rudder deflection initiating the turn and extends until the yawing moment generated by the distribution of forces acting on the hull and sail is balanced by the moment created by the lifting rudder. Note that this argument is ignoring the complicating factor of out-of-plane forcing for simplicity. The horizontal orientation of the vehicle, measured by the angle of drift  $\beta$ , is determined during this unsteady phase as the orientation which leads to a force distribution that balances the lifting rudder. The degree to which MVGs play a role in determining  $\beta$  during the unsteady phase by virtue of the hydrodynamic forces acting on the raised portions of the MVGs cannot be determined from a captive model test. The force and moment measurements show an increased transverse force of 1.72 lbs and an increased yaw moment of 1.84 ft-lbs during steady turning with MVGs present. This is consistent with increased lateral force on the MVGs during cross flow conditions. The steady drift angle that is ultimately determined during the course of the unsteady phase is critical to the resulting distribution of out of plane forces acting on the vehicle and therefore to the entire turning maneuver. An increased lateral force contribution by the MVGs which may alter  $\beta$  during the unsteady phase of a turning maneuver may be present but can only be verified by future testing with a free-running vehicle.

## CONCLUSIONS

Particle Image Velocimetry (PIV), a quantitative flow visualization technique, was utilized to characterize the flow field around a sting-mounted captive model in a steady turn. The submarine model (ONR Body-1) was also instrumented with block gages, yielding force and moment data in tandem with the detailed map of the cross-flow velocity field. The results indicated that in a mildly severe turn ( $r' = 0.53$ ), the interaction of the sail trailing vortex with the hull separated flow results in a net circulation around the body in such a way that the separation zone is rotated toward the deck of the model. Since the separation zone is an area of low pressure and a corresponding area of high pressure exists on the opposite side of the hull, this mechanism contributes to a net upward force on the hull aft of the sail. Because the area aft of the sail is for the most part aft of the CG, this net upward force results in a net downward pitching moment, consistent with observations.

Fitting MVGs on the top of the model results in a drastic change in the flow field around the model and in the measured vertical force and pitching moment. A prominent large-scale vortical structure with counter-clockwise (positive) circulation exists near the deck of the model as a result of tip vortices shed from the MVGs. Because this vortex is very near the body, it serves to bring high momentum fluid into this region of normally low pressure and will effectively reattach the boundary layer. This delay of flow separation on the deck in the aft results in a pressure recovery, netting the model a downward vertical force aft of the sail and a corresponding pitch-up moment.

The proposed mechanism that leads to the generation of out-of-plane forcing on the hull and the modification that arises from using MVGs could be further substantiated and verified with additional experimentation. This test concentrated on a single steady turn condition and relied on PIV measurements combined with total force and moment data. Of particular interest in a future experiment would be to supplement the above measurements with the simultaneous acquisition of surface pressures

at locations defined by a regularly spaced grid on the hull. Pressure measurements on the submarine's surface would provide an additional means to accurately describe regions of flow separation and provide information on the distribution of forces acting on the hull. The experiment should be extended to include a series of turning conditions (variation of turning radii, orientation and speed), and the experimental data should be compared with calculations from a Reynolds-Averaged Navier-Stokes (RANS) computer code. Distributed force information would also provide guidance on grid spacing issues required to correctly resolve submarine pitching and yawing moments with CFD codes. Comparison of CFD calculations with field measurements of velocity and surface pressures would serve to direct future code development and may also illuminate additional areas on which to focus experimental study.

Future experiments, on model submarines and in other naval applications, would also benefit from improvements to the PIV instrumentation. Ongoing efforts will allow PIV measurements on a much larger scale, making possible testing on larger-scale models such as the LSV1, LSV2 and even full-scale vehicles. Stereoscopic PIV, which would allow measurements of all three components of velocity in a plane is also being actively developed. For the current problem of cross-flow separation around a turning submarine, the coupling of PIV measurements with the acquisition of surface pressures, consideration of additional turning conditions, comparison with RANS calculations and improvements to the PIV configuration will provide additional fundamental insight into the complex mechanisms advanced in this paper.

The implementation of PIV in a large-scale Navy facility as an optical diagnostic to probe the highly complex, three-dimensional flow field near the hull of a maneuvering submarine has been successful. Instantaneous maps of velocity components at many points in a plane have permitted the computation of derivative quantities such as vorticity to provide physical insight into the origin of the out-of-plane forces acting on the vehicle. These detailed measurements of the flow field also provide valuable validation data for CFD codes and serve to stimulate future submarine designs. This experiment has demonstrated the tremendous potential of PIV and has shown that it has matured to the point where it can become a routine diagnostic for future naval applications.

## ACKNOWLEDGMENTS

The work described in this report could not have been done without the hard work and dedication of Dr. David Fry, Ms. Deborah Furey and Mr. David Mackintosh. Their effort and expertise are much appreciated. The authors would also like to thank: Dr. Joe Katz, of Johns Hopkins University, for use of his submersible PIV system, Dr. Jerome Feldman of NSWC for sharing his insights into submarine maneuvering, and Dr. In-Young Koh, of NSWC, Dr. Thomas Huang and Dr. Wade Miner of Newport News Shipbuilding for their support of this project.

## REFERENCES

1. Lin, J., T. Sedler, D. Stiver, W. Faller, and D. Hess, "Application of Micro-Vortex Generators For Submarine Maneuvering Enhancement," International Symposium On Seawater Drag Reduction, 22-24 July 1998, Naval Undersea Warfare Center, Newport, RI,.. (1998).
2. Liu, H. L. and T. Fu, "PIV Measurement of Vortical Structures in the DTMB Rotating Arm Facility," Carderock Division, Naval Surface Warfare Center, Hydromechanics Directorate Research & Development Report, CRDKNSWC/HD-1416-02, (1994).
3. Bertuccioli, L., G.I. Roth, J. Katz, and T.R. Osborn, "Turbulence Measurements In The Bottom Boundary Layer Using Particle Image Velocimetry," Journal of Atmospheric and Oceanographic Technology, **16**(11), Part 1, 1635-1646 (1999).
4. Sinha, M. and J. Katz, "Quantitative Visualization of The Flow in A Centrifugal Pump with Diffuser Vanes, Part A: On Flow Structure and Turbulence," Journal of Fluids Engineering, **122**(1), 97-107 (2000).
5. Adrian, R.J., "Particle-imaging Techniques for experimental fluid mechanics," Annual Review of Fluid Mechanics, **23**, 261-304 (1991).
6. Grant, I., "Particle Image Velocimetry: A Review," J. Mech. Eng. Sci., **211**(1), 55-76 (1997).
7. "Nomenclature for Treating the Motion of a Submerged Body Through a Fluid," Report of the American Towing Tank Conference prepared by the Hydromechanics Subcommittee of the Technical and Research Committee of the Society of Naval Architects and Marine Engineers, Technical and Research Bulletin No. 1-5 (Apr 1950).
8. Coleman, Hugh W. and W. Glenn Steele, Experimentation and Uncertainty Analysis for Engineers, John Wiley and Sons, New York (1989).

**THIS PAGE INTENTIONALLY LEFT BLANK**

## INITIAL DISTRIBUTION

			Center Distribution		
Copies	Code	Name	Copies	Code	Name
1	NAVSEA		1	50	Webster
1	05H2	King	1	5060	Walden
1	05H	Merrill	1	5200	Stenson
1	JHU		1	5300	Furey
1		Katz	1	5300	Pickett
1	NNS CC		1	5400	Fry
1		Huang	1	5400	Remmers
3	NNS		1	5500	Applebee
1		Miner	1	5600	Koh
1		Sedler	1	5600	Ammeen
1		Smith	1	5600	Bedel
2	DTIC		1	5600	Bochinski
			1	5600	Nigon
			1	5600	Feldman
			1	5600	Mackintosh
			1	5600	Moran
			1	5600	Roddy
			1	3441	Congedo
			1	7250	Roth

**THIS PAGE INTENTIONALLY LEFT BLANK**